Journal of Cutaneous Pathology

WILEY

ORIGINAL ARTICLE OPEN ACCESS

Multiplexed Immunofluorescent Characterization of T-Cell and Myeloid Cell Populations Reveals Histologic Subtype Differences Within the Immunosuppressive Landscape of Human Basal Cell Carcinoma

Alan S. Shen[1] | Lauren E. Heusinkveld[2] | Ajay Zalavadia[3] | Andrelie Branicky[3] | Sanjay Anand[1,4] | Melissa Piliang[5,6] | Edward V. Maytin[1,4,6]

[1]Cleveland Clinic Lerner College of Medicine of Case Western Reserve University, Cleveland, Ohio, USA | [2]Department of Pathology, Mass General Brigham, Harvard Medical School, Boston, Massachusetts, USA | [3]Cleveland Clinic Lerner Research Institute Imaging Core, Cleveland, Ohio, USA | [4]Department of Biomedical Engineering, Cleveland Clinic, Cleveland, Ohio, USA | [5]Department of Pathology, Cleveland Clinic, Cleveland, Ohio, USA | [6]Department of Dermatology, Cleveland Clinic, Cleveland, Ohio, USA

Correspondence: Edward V. Maytin (maytine@ccf.org)

Received: 6 June 2025 | **Revised:** 18 December 2025 | **Accepted:** 13 March 2026

Keywords: basal cell carcinoma | immunofluorescence microscopy | immunosuppression | tumor-associated macrophages | tumor-infiltrating lymphocytes

ABSTRACT

Background: Basal cell carcinomas (BCCs) are thought to reside within an immunosuppressed tumor microenvironment, but a detailed characterization of BCC-associated immune cells was lacking.

Methods: Utilizing multiplex immunohistochemistry (IHC) (Vectra Polaris, Akoya Biosciences), we designed two staining panels, targeting either T cells (CD3, CD4, CD8, FoxP3, PD1) or myeloid cells (neutrophil elastase, CD68, CD163, HLADR, CD1c). Formalin-fixed paraffin-embedded (FFPE) BCC tumor specimens ($n = 30$) were analyzed using the panels. The majority of immune cells reside at the peritumoral margin; therefore, a boundary zone of 150 μm around tumor nests was used to capture them.

Results: A CD8/T-reg ratio and M1/M2 macrophage ratio of < 0.5 was observed across all BCC specimens, confirming an overall immunosuppressive phenotype. Among different histologic subtypes, infiltrative BCC had significantly lower CD8 T cells ($p = 0.038$), T-regulatory cells ($p = 0.039$), and CD8/T-reg ratio ($p = 0.048$), as well as lower M1/M2 ratio ($p = 0.034$) compared to non-infiltrative BCC subtypes.

Conclusions: The association of infiltrative BCC with a more immunosuppressed microenvironment may contribute to more aggressive biological behavior. Overall, these data demonstrate a method to determine T cell and myeloid profiles in fixed FFPE skin tumor tissues that can identify subtle immune profile differences.

1 | Introduction

Basal cell carcinoma (BCC) is the most common human malignancy, comprising up to 80% of all skin cancers [1] and affecting ~2 million individuals annually in the United States [2]. BCCs comprise multiple histologic subtypes, and many lesions exhibit more than one histologic pattern [2]. The less aggressive subtypes include nodular and superficial BCCs, which have limited dermal invasion [3], while more aggressive lesions include morpheaform, micronodular, basosquamous, and infiltrative subtypes that more often exhibit single cell invasion, lymphovascular penetration, and perineural invasion, as well as a dense, fibrotic stroma [4, 5].

While BCC pathogenesis is driven by environmental and genetic factors, most notably chronic ultraviolet (UV) radiation

---

Journal of Cutaneous Pathology, 2026; 0:1–9
https://doi.org/10.1111/cup.70098

exposure and dysregulation of Hedgehog pathway signaling [3], a critical role for the tumor immune microenvironment (TME) in the pathogenesis, aggressiveness, and therapeutic resistance of BCC has only been recognized recently. The BCC TME is very complex and exhibits a Th2-skewed cytokine profile [6, 7], with elevated levels of IL-4, IL-10, and IL-13 supporting the development of an immunosuppressive milieu marked by abundant regulatory T cells (T-regs) [8] and relatively few cytotoxic T lymphocytes (CTLs) [9]. Nearly 45% of CD4$^+$ T cells in the BCC peritumoral stroma can be T-regs (FoxP3$^+$ T cells) [10]. From a myeloid perspective, the BCC TME is dominated by M2-polarized macrophages [9], which outnumber their antitumor M1 counterparts. These M2 macrophages contribute to immune evasion by secreting immunosuppressive cytokines (e.g., TGF-β), promoting angiogenesis, and suppressing CTL activity [11]. In addition to elevated TGF-β, some studies have shown reduced CD1a$^+$ Langerhans cells and an absence of mature dendritic cells (DCs) in BCC tumors [12]. The predominantly immunosuppressive features of the BCC TME are accompanied by epigenetic downregulation of the antigen presentation machinery [13], which together may hinder tumor regression and contribute to lesion recurrence.

Notably, while some immunosuppressive aspects of the BCC TME have been characterized, data on the cellular composition of TME as a function of BCC histologic subtype remain limited. Given that BCCs of different subtypes differ in their invasive behavior, the elucidation of immunocellular differences could uncover a previously unappreciated driver of tumor aggressiveness and suggest which BCC subtypes might benefit from immunomodulatory therapies. In this study, we employed a multiplex immunofluorescence platform to characterize T cell and myeloid subsets across histologic subtypes in BCC.

2 | Methods

2.1 | BCC Sample Requisition

Formalin-fixed paraffin-embedded (FFPE) BCC diagnostic biopsy samples from 30 separate patients were obtained from the Pathology Department at the Cleveland Clinic, under an IRB-exempt tissue acquisition protocol in which specimens were fully de-identified and stripped of any associated clinical information. Tumor presence and histologic subtypes were confirmed by a board-certified dermatopathologist.

2.2 | Multiplex Immunofluorescence Staining

FFPE tissues were stained using T-cell and myeloid cell antibody panels and the Ventana Discovery ULTRA automated stainer from Roche Diagnostics (Indianapolis, IN, USA). In brief, antigen retrieval was performed using a tris/borate/EDTA buffer (Discovery CC1, 06414575001; Roche), pH 8.0–8.5 at 95°C for 48 min. Incubation times for the antibodies listed below were 16 min to 1 h. Antigen denaturing was performed using a citrate buffer (Discovery CC2, 05424542001; Roche) between each antibody incubation step. The antibodies were visualized using the OmniMap anti-Rabbit HRP (05269679001; Roche) and OmniMap anti-Mouse HRP (05269652001; Roche), in conjunction with the Akoya Biosciences (Marlborough, MA, USA). Opal fluorophores that are listed with their respective antibodies below.

For the T-cell panel, the following six antibodies were sequentially applied along with their respective dilutions and conjugated opal fluorophore: (1) CD4 (predilute, 05552797001; Roche) Opal 570 (FP1488001; Akoya); (2) PD-1 (1:250, ab137132; Abcam) Opal 620 (FP1495001; Akoya); (3) CD8 (predilute, 05937248001; Roche) Opal 480 (FP1495001; Akoya); (4) FOXP3 (1:00, ab20034; Abcam) Opal 520 (FP14870011; Akoya); (5) CD3 (predilute, 05278422001; Roche) Opal 690 (FP1497001; Akoya); and (6) anti-Pan keratin (predilute, 05267145001; Roche) Styramide 750 (45065; AAT Bioquest). For the myeloid cell panel, the following six antibodies were sequentially applied: (1) CD68 (predilute, 05278252001; Roche) Opal 480 (FP1495001; Akoya); (2) CD1c (1:150, ab246520; Abcam) Opal 690 (FP1497001; Akoya); (3) neutrophil elastase (1:50, ab68672; Abcam) Opal 570 (FP1488001; Akoya); (4) HLA-DR (1:150, 14-9956-82; Invitrogen) Opal 620 (FP1495001; Akoya); (5) CD163 (predilute, ab74604; Abcam) Opal 520 (FP1487001; Akoya); and (6) the anti-pan keratin conjugate previously listed above. Further information regarding antigens and fluorophores is available in Table S1. The slides were counterstained with Spectral DAPI (FP1490; Akoya Biosciences) and mounted with ProLong Gold mounting medium (P36930; Invitrogen).

2.3 | Slide Analysis

Multispectral scans of whole-mounted slides were acquired using the Vectra Polaris Automated Quantitative Pathology Imaging System (Akoya Biosciences), followed by spectral unmixing with InForm software (Version 2.4.1, Akoya Biosciences) to separate Opal dyes and tissue autofluorescence. Intensity thresholds to reliably detect each of the fluorophores in the T-cell or myeloid cell panel were calibrated from stained tissue standards (tonsillar lymphoid tissue). Tiles of the spectrally unmixed component data were then stitched into whole slide images and saved as OME-TIFF files using an open-source software package, QuPath [14]. While using QPath to analyze the spectrally unmixed images of BCC specimens, pan cytokeratin staining and examination of an adjacent H&E-stained section were used as guides to annotate the boundaries of the BCC tumor (region of interest [ROI]). The peritumoral margin, where most of the immune cells were located, was defined by expanding the tumor ROI boundary outward by 150 μm, while excluding epidermal regions. We evaluated multiple distances across several samples and found that 150 μm was the largest radius that consistently encompassed the predominant immune cell band surrounding tumor nodules. Extending this radius any further led to the inclusion of immune cells associated with adjacent skin structures (e.g., hair follicles, sebaceous glands), rather than immune cells likely to be involved in antitumor activity.

Detection of cells within the tumor ROI and peritumoral ROI was performed using a deep-learning-based method, StarDist [15], and a pretrained model. Using the model, nuclear stain DAPI was first used to detect nuclei in fluorescence images.

Next, steps to remove nuclei with minimal DAPI intensity and nuclei outside the size range of 10–250 μm^2 were employed to minimize detection artifacts. Finally, cells were classified using a threshold-based method for each marker, along with a decision tree for T cells and for myeloid cells (see below) [16].

2.4 | Immune Cell Definitions

Using the T-cell and myeloid panels, individual immune cells were defined as follows. For the T-cell panel, total T cells ($CD3^+$), cytotoxic T cells ($CD3^+$, $CD8^+$), helper T cells ($CD3^+$, $CD4^+$), exhausted T cells ($CD3^+$, $PD\text{-}1^+$), and T-regs ($CD3^+$, $CD4^+$, $FoxP3^+$) were identified. The decision tree used to classify immune cells labeled by the T-cell antibody panel [16] is shown in Figure S1.

For the myeloid panel, total macrophages ($CD68^+$), M1 macrophages ($CD68^+$, $HLA\text{-}DR^+$), M2 macrophages ($CD68^+$, $CD163^+$), neutrophils (neutrophil elastase$^+$), and dendritic cells ($CD1c^+$) were identified. BCC tumor nests were identified as $PanCK^+$. The decision tree used to classify immune cells labeled by the myeloid cell antibody panel [16] is shown in Figure S2.

2.5 | Immune Cell Percentages

Individual immune cell subsets identified by the T-cell and myeloid panels were quantified as a percentage of total T cells or total myeloid cells, respectively. Total T cells were defined as all $CD3^+$ cells (Figure S1), while total myeloid cells included M1 and M2 macrophages, “other” macrophage subsets, DCs, and neutrophils (Figure S2).

To further characterize the BCC immune infiltrate, cellular ratios such as M1/M2 and $CD8^+$/T-reg were calculated by dividing the absolute counts of M1 macrophages or $CD8^+$ T cells by the counts of M2 macrophages or T-regs, respectively.

2.6 | BCC Histologic Subtype Classifications

Most BCC specimens exhibited mixed histology, with more than one subtype. A complete list of BCC samples and the histological subtypes diagnosed for each is provided in Table S2. For analytic purposes, any BCC with two or more subtypes was reassigned as having the most biologically aggressive subtype; for example, “infiltrative and nodular” was reclassified as “infiltrative.” In the final analysis, BCC tumors were categorized into two histologic groups, *infiltrative BCC* versus *non-infiltrative BCC* (see Section 3).

2.7 | Depth of Invasion

Depth of invasion (DOI) was assessed on H&E-stained slides from each BCC specimen, using QuPath software [14]. DOI was defined as the perpendicular distance from the granular layer of the epidermis to the bottom of the deepest tumor nest, in micrometers (μm). For each specimen, 10 evenly spaced measurements were taken across the entire tumor section; the average DOI and the largest (maximum) DOI were recorded.

2.8 | Statistical Analysis

A Mann–Whitney U test was used to compare cellular ratios between infiltrative and non-infiltrative groups. Adjustment for multiple comparisons was not performed, as these analyses were primarily exploratory, and the cellular ratios of interest (i.e., CD8/CD4 T cells; CD8/T-reg T cells; M1/M2 macrophages) were prespecified before analysis. A $p < 0.05$ was considered significant.

3 | Results

Of the 30 BCC specimens stained with the T-cell and myeloid antibody panels, 30 of 30 were included in the final myeloid cell analysis and 29 of 30 in the T-cell analysis (with one sample excluded due to poor DAPI staining). Representative images are shown for T cells in Figure 1 and myeloid cells in Figure 2. Each figure shows the appearance of the original H&E tumor section (Figures 1A and 2A), the spectrally unmixed image after the tumor ROI and peritumoral ROI have been delineated (Figures 1B and 2B), and magnified sections of regions before and after computer-assisted classification analysis (Figures 1C and 2C, left and right panels, respectively). Once classified, all cells of each type were tallied to define the immune cell populations that characterized the TME for each BCC.

During collective analysis, ratios of immune cell subtypes were indicative of immunosuppression (Figure 3). Thus, the CD8/T-reg ratio (mean = 0.57, Figure 3A) and M1/M2 macrophage ratio (mean = 0.38, Figure 3B) were both less than one, indicating a predominance of CD4 T cells and regulatory T cells over CD8 T cells, and a higher abundance of M2 macrophages compared to M1 macrophages across the entire cohort.

When cohorts were stratified by histologic subtype, infiltrative BCCs ($n = 10$) exhibited a significantly lower CD8/T-reg ratio compared to non-infiltrative ($n = 19$) subtypes ($p = 0.04$, Figure 4A). Analysis of individual cell populations showed that the proportion of CD8 T cells among total T cells was significantly lower in the infiltrative group ($p = 0.03$, Figure 4B), while the proportion of T-regs was significantly higher ($p = 0.04$, Figure 4D). No significant differences were observed in the proportions of CD4 T cells (Figure 4C) or PD-1-expressing T cells (Figure 4E) between the BCC subtypes.

For myeloid cells, infiltrative BCCs ($n = 11$) demonstrated a significantly lower M1/M2 macrophage ratio compared to non-infiltrative ($n = 19$) subtypes ($p = 0.01$, Figure 5A). Although not statistically significant, infiltrative subtypes tended to have lower proportions of M1 macrophages (Figure 5B) and higher proportions of M2 macrophages (Figure 5C) among total myeloid cells. No significant differences between infiltrative and non-infiltrative BCC were observed in the proportions of DCs (Figure 5D) or neutrophils (Figure 5E) among total myeloid cells.

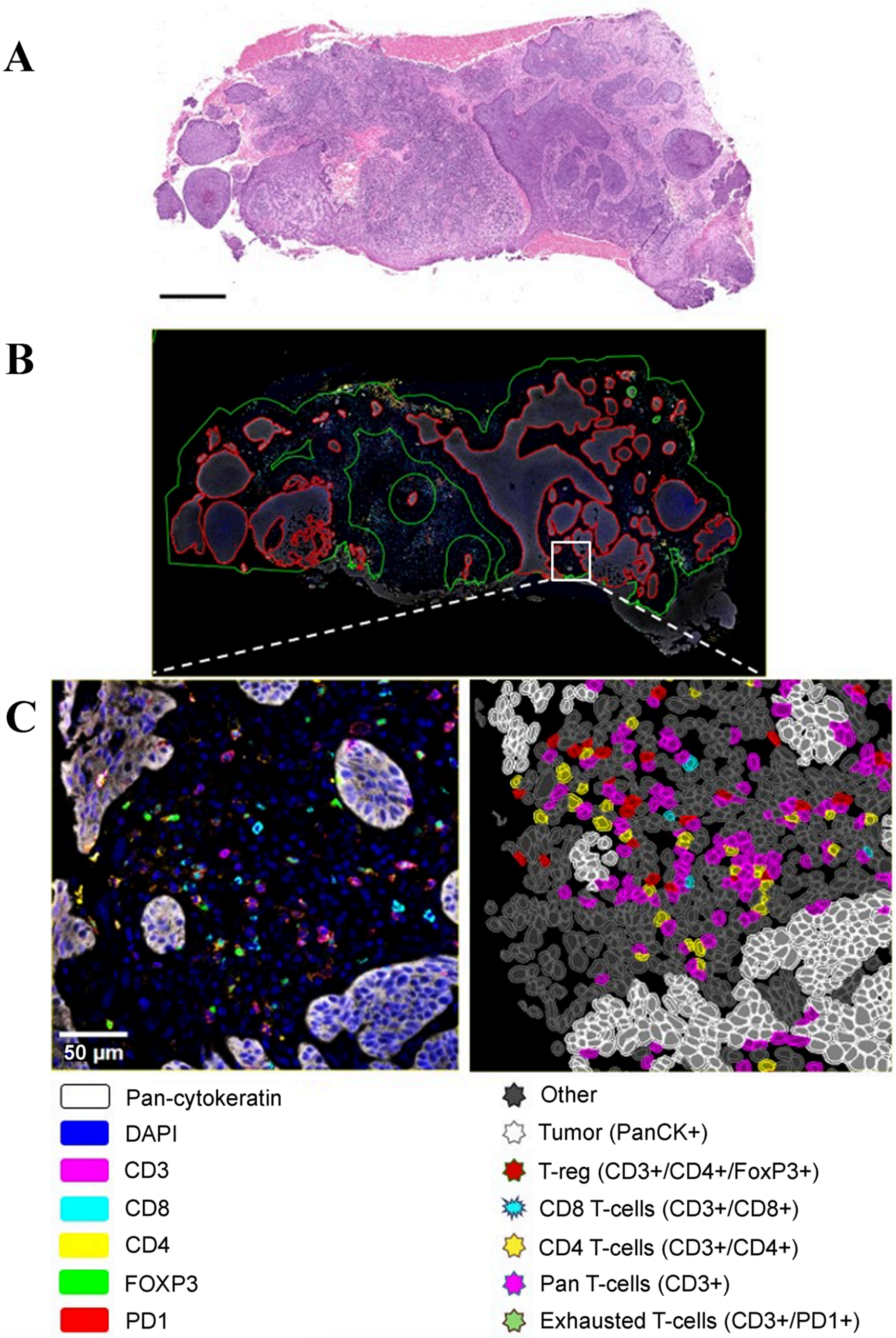

FIGURE 1 | Representative staining of BCC using the T-cell antibody panel. (A), Adjacent tissue section stained with H&E to show tumor morphology. Scale bar = 500 μm. (B) Computer algorithm-based tracing of tumor nests (red) and peritumoral margin (green). (C) Immunofluorescence staining of cells with each T-cell panel marker (left), alongside computer-aided identification of individual T-cell subtypes in the same field of view (right). Scale bar = 50 μm.

When stratifying BCC samples by anatomical location, tumors on the head and neck exhibited lower CD8/T-reg and M1/M2 macrophage ratios compared to those on the trunk and extremities (Figure S3). However, these differences were not statistically significant.

When correlating CD8/T-reg and M1/M2 ratios with DOI, no significant associations were observed. The average DOI among infiltrative BCC samples was 1575 μm, compared to 1397 μm in non-infiltrative BCC samples (data not shown).

4 | Discussion

Increasing evidence suggests that the TME of BCC plays a critical role in tumor aggressiveness and resistance to therapy. In

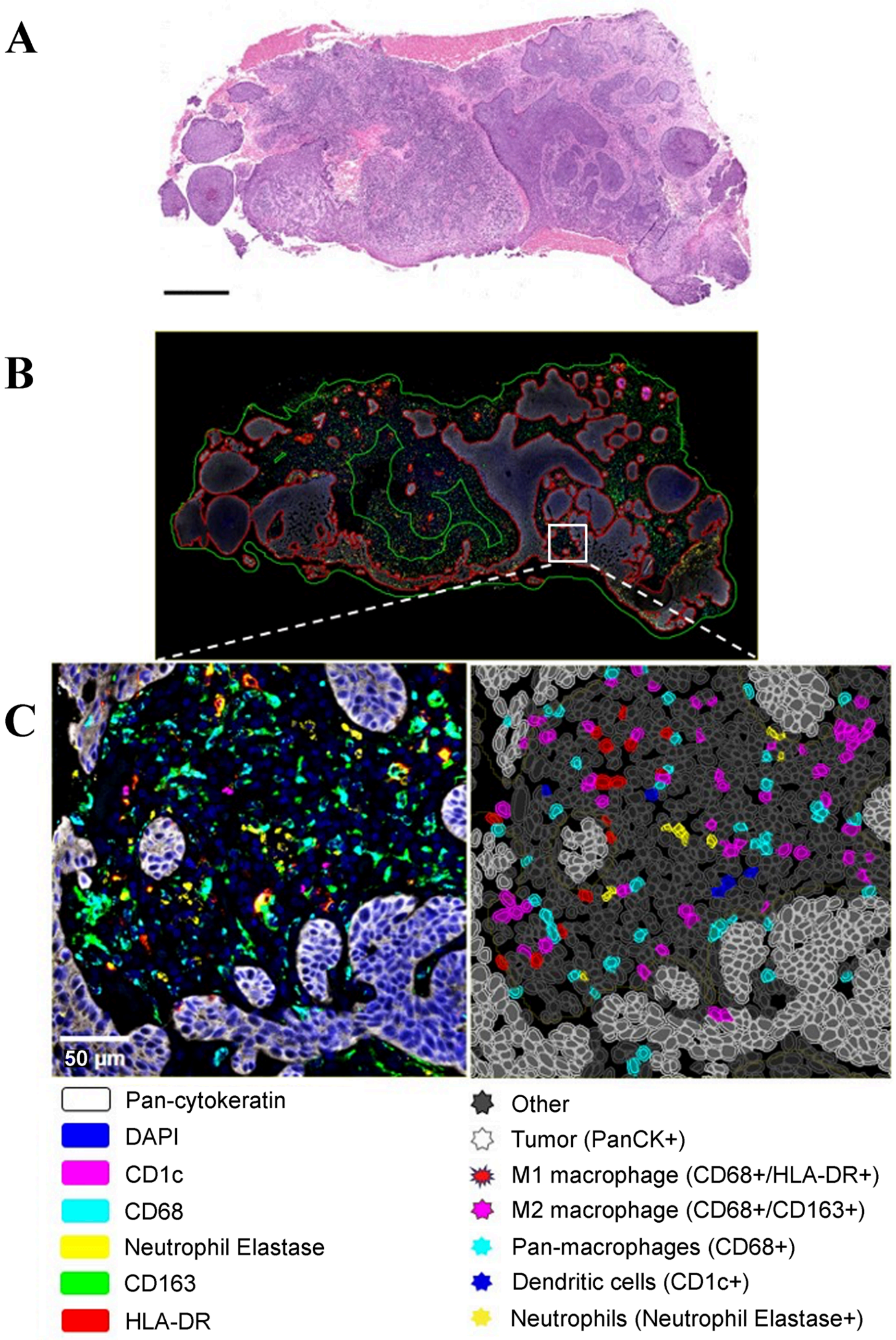

FIGURE 2 | Representative staining of BCC using the myeloid cell antibody panel. (A) Adjacent tissue section stained with H&E. Scale bar = 500 μm. (B) Computer algorithm-based tracing of tumor nests (red) and peritumoral margin (green). (C) Immunofluorescence staining of cells with each myeloid cell panel marker (left), alongside computer-aided identification of individual myeloid cell subtypes in the same field of view (right). Scale bar = 50 μm.

this study, we have confirmed and extended the evidence from prior studies by characterizing the cellular components of the BCC TME in a sample set from 30 BCC patients. The data reveal low values for the CD8/T-reg ratio and the M1/M2 macrophage ratio (0.57 and 0.38, respectively), indicative of a relative abundance of immunosuppressive cell populations. These ratios carry clinical relevance. In other solid tumors, lower CD8/T-reg ratios have been associated with higher tumor grade, poorer prognosis, and reduced response to treatment. Specifically, in urothelial carcinoma, a CD8/T-reg ratio below 1.0 correlated with minimal response to treatment [17], highlighting its predictive value. Similarly, reduced M1/M2 macrophage ratios have been linked to worse outcomes across various malignancies [18], including gastric cancer, where a ratio below 1.16 predicted significantly shorter overall survival [19]. In the context of BCC, our findings reinforce the relevance of immunosuppressive cell ratios as potential biomarkers of tumor behavior and therapeutic response.

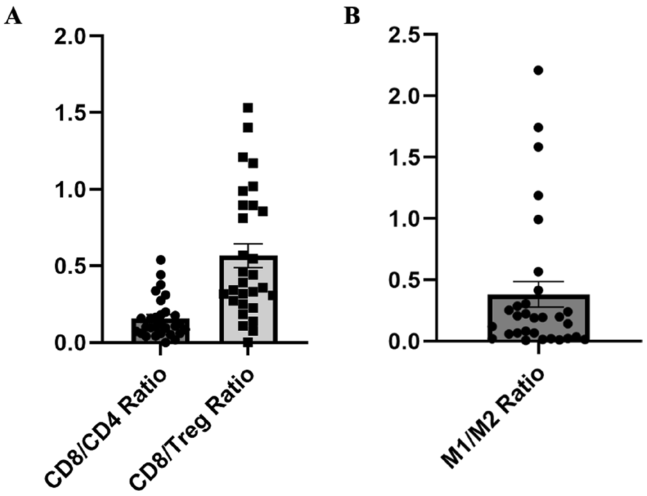

FIGURE 3 | Overall ratios of immune cell subtypes among all BCC samples. (A) CD8/CD4 ratio and CD8/T-reg ratio. (B) M1/M2 macrophage ratio.

Our study demonstrated differences in the TME that were dependent upon histological BCC subtype. Among BCC histological subtypes, infiltrative variants are considered more aggressive due to their invasive growth patterns, higher recurrence rates, and worse response to therapy [20]. However, before now, few studies had explored how the immune landscape varies across different BCC subtypes. The notion that immunosuppressive cells within BCC might influence tumor invasiveness is supported by a prior report showing that M2 macrophages promote BCC invasion and angiogenesis through COX-2-dependent mechanisms [21]. In addition, cytokine profiling studies have shown that more aggressive BCC variants and tumors on the head and neck are associated with higher levels of Th2 cytokines [22], and morphologically aggressive subtypes exhibit denser, fibrotic stromal patterns [5]. In the current study, stratifying BCCs by histologic subtype revealed that tumors with infiltrative features exhibited significantly lower CD8/T-reg and M1/M2 ratios compared to non-infiltrative subtypes, pointing to a functionally more immunosuppressive TME in aggressive variants. These findings may help explain the worse postsurgical

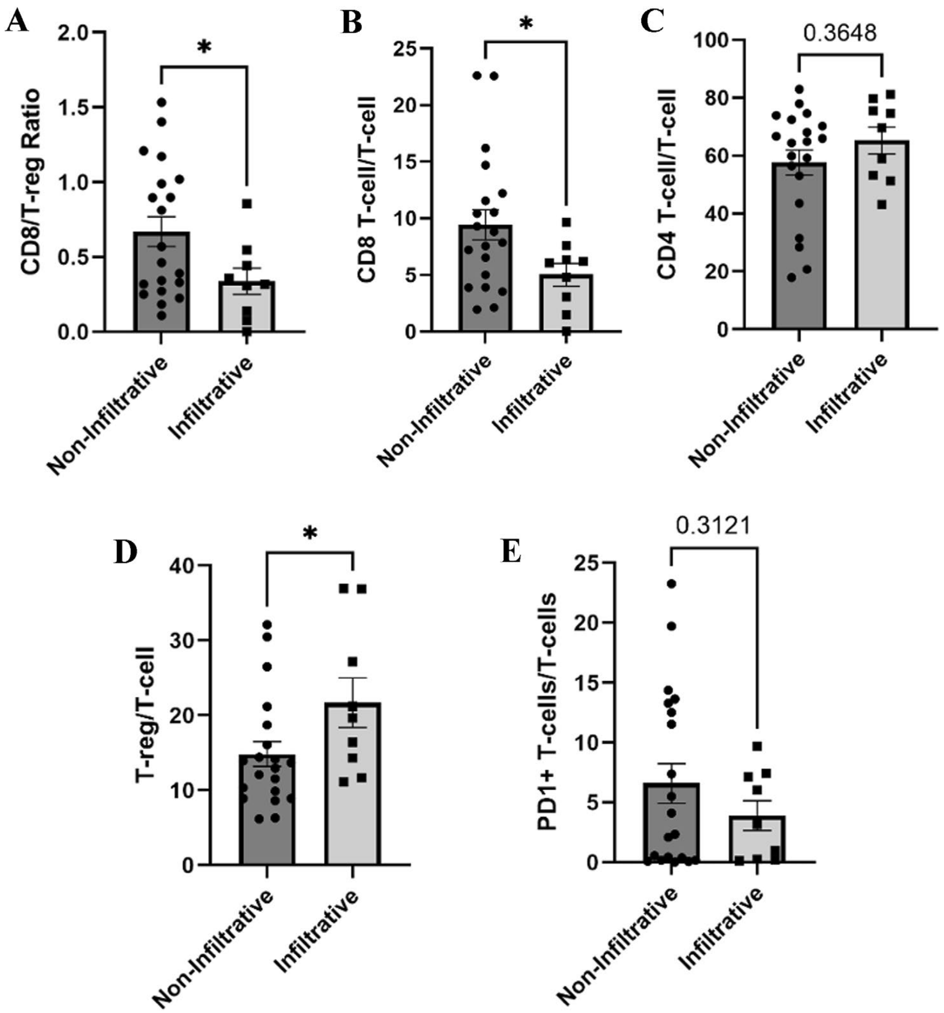

FIGURE 4 | Ratios and proportions of various T-cell subtypes in the peritumoral stroma of BCC with an infiltrative vs. non-infiltrative histological subtype. (A) Ratio of $CD8^+$ T cells (cytotoxic) versus regulatory T cells (T-regs). Graphs in (B–E) show the proportion of CD8 T cells (B), CD4 T cells (C), T-regs (D), and exhausted T cells (E) relative to total $CD3^+$ T cells. $*p < 0.05$.

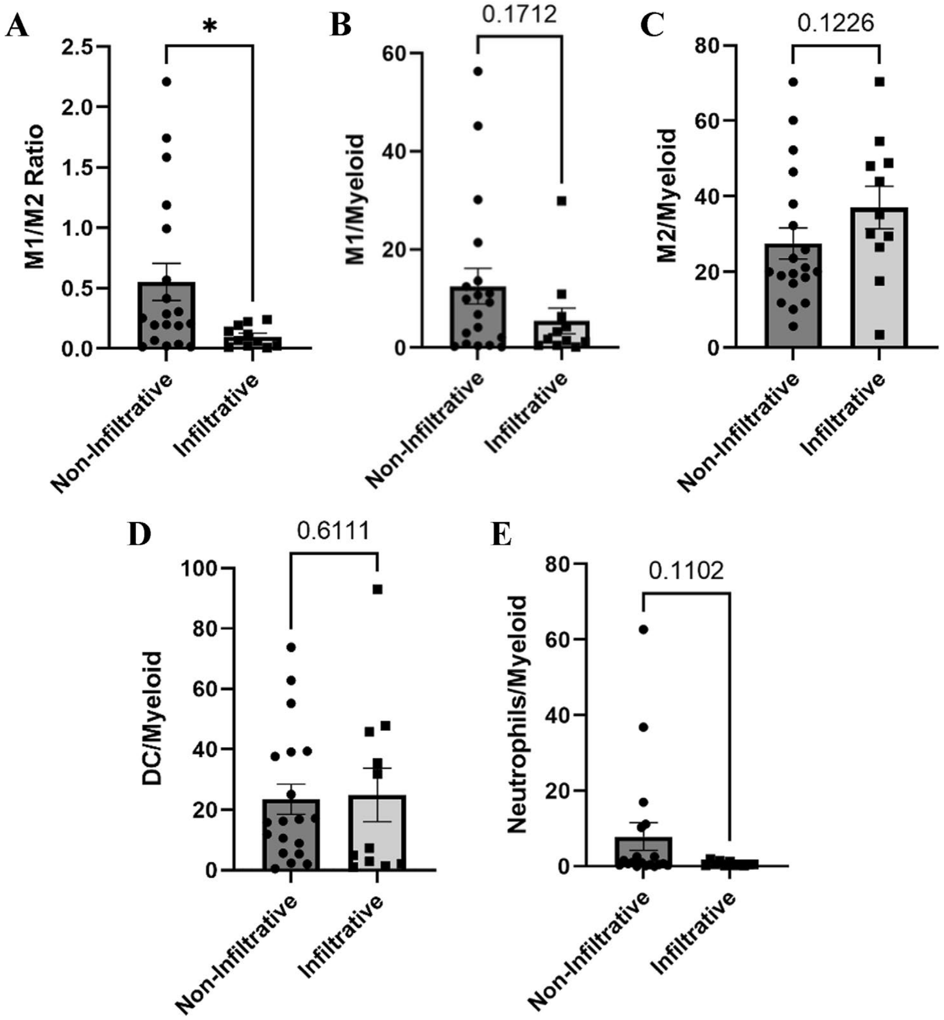

FIGURE 5 | Ratios and proportions of myeloid cell subtypes in the peritumoral stroma of BCC with an infiltrative versus non-infiltrative histological subtype. (A) M1/M2 macrophage ratio. Graphs in (B–E) show the proportion of M1 macrophages (B), M2 macrophages (C), dendritic cells (D), and neutrophils (E) relative to all myeloid cells. *$p < 0.05$.

outcomes of infiltrative BCCs [20], in which impaired antitumor immunity might hamper tumor cell clearance.

No significant role for neutrophils was observed in this study, which may reflect the generally low neutrophil abundance in tissues under quiescent conditions, whereas neutrophils are typically recruited after an inflammatory insult [23]. Similarly, the proportion of DCs was not significantly different between subtypes. We expect that a more detailed phenotyping of DC subsets (to include immature, cross-presenting, skin-resident Langerhans cells, etc.) may uncover relevant functional differences, since prior work showed that BCC lesions have relatively high levels of immature DCs and a paucity of Langerhans cells, most likely contributing to local immunosuppression [8].

In addition, we did not observe differences in PD-1 expression on T cells across histologic subtypes. This may reflect our sample size or the possibility that PD-1 dynamics are more pronounced in treatment-related contexts. We also note that PD-L1 was not included in our current panel; incorporating this marker into expanded future panels will allow us to more fully characterize PD-L1 expression on tumor cells and myeloid populations and its potential role in modulating local T-cell activity within the TME.

Immunologic differences between BCC subtypes may have therapeutic implications. Treatments such as imiquimod and photodynamic therapy (PDT), both of which stimulate antitumor immunity [7, 24], may be particularly effective in BCCs with a highly immunosuppressive TME (a hypothesis we hope to test in the future).

In this study, we also asked how CD8/T-reg and M1/M2 macrophage ratios varied by body site. Although not statistically significant, BCCs on the head and neck exhibited numerically lower CD8/T-reg and M1/M2 ratios compared to those on the trunk or extremities, suggesting a more immunosuppressive microenvironment for head and neck BCCs. This trend may help explain a higher propensity for recurrence and more aggressive behavior of BCC at these locations [25, 26].

Finally, we did not observe significant associations between BCC DOI and CD8/T-reg or M1/M2 macrophage ratios. This may in part reflect the predominance of mixed histologic subtypes in our cohort and the relatively small differences in DOI between infiltrative and non-infiltrative BCC groups. An important future direction will be to further evaluate how tumor burden relates to immune cell composition in larger, more subtype-specific datasets.

There are strengths and weaknesses of this study. A key strength is the use of multiplex immunofluorescence to provide more comprehensive and spatially resolved immune profiling compared to traditional IHC. Unlike traditional single-chromogen IHC, multiplex staining enables visualization and quantification of multiple immune populations within a single section, allowing the direct calculation of immune cell ratios such as CD8/T-reg and M1/M2. This offers more nuanced insight into the immunological balance within the TME. Previous studies of BCC TME mostly relied on single-marker IHC, limiting the ability to assess immune interrelationships. A limitation of our study is a lack of patient-level clinical data, preventing us from correlating immune features with treatment history or outcomes. Because they were derived from diagnostic biopsies, most of our samples were likely treatment-naïve, but this cannot be confirmed. We also did not have information on the patients' systemic immune status (e.g., chronic immunosuppression, concurrent malignancies), which may have introduced additional confounding effects. In addition, the relatively small sample size may have precluded the detection of subtle immune differences between subtypes or rare cell populations.

In future studies with larger sample sizes, we aim to incorporate additional markers to more granularly characterize T-cell subpopulations (e.g., memory, activated subsets), which were not examined in depth here. We also plan to further evaluate spatial immune–tumor interactions across histologic subtypes by assessing the extent to which immune cells directly engage with tumor cells within the local TME.

In conclusion, our findings demonstrate that infiltrative BCC subtypes exhibit a relatively more immunosuppressive TME than other subtypes, characterized by lower CD8/T-reg and M1/M2 ratios, which may contribute to clinical aggressiveness and recurrence of these tumors. Understanding the immunologic distinctions between BCC subtypes may inform the development of subtype-specific therapeutic strategies and improve the integration of immunotherapy into the treatment of high-risk BCC.

Author Contributions

Study conception and design: Alan S. Shen, Lauren E. Heusinkveld, and Edward V. Maytin. Acquisition, analysis, and interpretation of data: Alan S. Shen, Lauren E. Heusinkveld, Melissa Piliang, and Sanjay Anand. Analysis of data: Alan S. Shen, Lauren E. Heusinkveld, and Ajay Zalavadia. Supervision: Edward V. Maytin. Technical support: Andrelie Branicky. Formal analysis and writing – original draft preparation: Alan S. Shen, Ajay Zalavadia, and Edward V. Maytin. All authors contributed to the critical revision of the manuscript for important intellectual content and approved the final version.

Acknowledgments

We thank Dr. Tayyaba Hasan for longstanding collaboration on the NIH/NCI Program Project grant referenced above. We thank Dr. Judy Drazba, PhD, for her efforts in establishing the Digital Imaging Core at Cleveland Clinic that was central to this work.

Funding

This work was supported by the National Institutes of Health (R01 CA204158 and P01 CA084203).

Ethics Statement

This study was approved by Cleveland Clinic's Institutional Review Board (ID# 21-959).

Conflicts of Interest

The authors declare no conflicts of interest.

Data Availability Statement

The data that support the findings of this study are available on request from the corresponding author. The data are not publicly available due to privacy or ethical restrictions.

References

1. A. H. Roky, M. M. Islam, A. M. F. Ahasan, et al., "Overview of Skin Cancer Types and Prevalence Rates Across Continents," *Cancer Pathogenesis and Therapy* 3, no. 2 (2025): 89–100.

2. M. C. Cameron, E. Lee, B. P. Hibler, et al., "Basal Cell Carcinoma: Epidemiology; Pathophysiology; Clinical and Histological Subtypes; and Disease Associations," *Journal of the American Academy of Dermatology* 80, no. 2 (2019): 303–317.

3. J. Pyne, D. Sapkota, and J. C. Wong, "Aggressive Basal Cell Carcinoma: Dermatoscopy Vascular Features as Clues to the Diagnosis," *Dermatology Practical & Conceptual* 2, no. 3 (2012): 203a02.

4. C. Requena, C. Serra-Guillen, and O. Sanmartin, "Histologically Agressive Basal Cell Carcinoma With Particular Emphasis on Galeal Infiltration of the Scalp," *Actas Dermo-Sifiliográficas* 113, no. 6 (2022): 575–582.

5. P. Kaur, M. Mulvaney, and J. A. Carlson, "Basal Cell Carcinoma Progression Correlates With Host Immune Response and Stromal Alterations: A Histologic Analysis," *American Journal of Dermatopathology* 28, no. 4 (2006): 293–307.

6. E. Chiang, H. Stafford, J. Buell, et al., "Review of the Tumor Microenvironment in Basal and Squamous Cell Carcinoma," *Cancers* 15, no. 9 (2023): 2453.

7. C. Zilberg, J. G. Lyons, R. Gupta, and D. L. Damian, "The Immune Microenvironment in Basal Cell Carcinoma," *Annals of Dermatology* 35, no. 4 (2023): 243–255.

8. H. G. Kaporis, E. Guttman-Yassky, M. A. Lowes, et al., "Human Basal Cell Carcinoma Is Associated With Foxp3$^+$ T Cells in a Th2 Dominant Microenvironment," *Journal of Investigative Dermatology* 127, no. 10 (2007): 2391–2398.

9. B. Beksac, N. Ilter, O. Erdem, P. Cakmak, S. Cenetoglu, and D. Yapar, "Sparsity of Dendritic Cells and Cytotoxic T Cells in Tumor Microenvironment May Lead to Recurrence in Basal Cell Carcinoma," *International Journal of Dermatology* 59, no. 10 (2020): 1258–1263.

10. S. H. Omland, P. S. Nielsen, L. M. Gjerdrum, and R. Gniadecki, "Immunosuppressive Environment in Basal Cell Carcinoma: The Role of Regulatory T Cells," *Acta Dermato-Venereologica* 96, no. 7 (2016): 917–921.

11. J. Liu, X. Geng, J. Hou, and G. Wu, "New Insights Into M1/M2 Macrophages: Key Modulators in Cancer Progression," *Cancer Cell International* 21, no. 1 (2021): 389.

12. S. H. Omland, “Local Immune Response in Cutaneous Basal Cell Carcinoma,” *Danish Medical Journal* 64, no. 10 (2017): B5412.

13. T. Oka, S. S. Smith, V. S. Oliver-Garcia, et al., “Epigenomic Regulation of Stemness Contributes to the Low Immunogenicity of the Most Mutated Human Cancer,” *Cell Reports* 44 (2025): 115561.

14. P. Bankhead, M. B. Loughrey, J. A. Fernandez, et al., “QuPath: Open Source Software for Digital Pathology Image Analysis,” *Scientific Reports* 7, no. 1 (2017): 16878.

15. U. Schmidt, M. Weigert, C. Broaddus, and G. Myers, “Cell Detection With Star-Convex Polygons,” paper presented at International Conference on Medical Image Computing and Computer-Assisted Intevention (MIDDAI), Granada, Spain, September 16–20, 2018.

16. A. Viratham Pulsawatdi, S. G. Craig, V. Bingham, et al., “A Robust Multiplex Immunofluorescence and Digital Pathology Workflow for the Characterisation of the Tumour Immune Microenvironment,” *Molecular Oncology* 14, no. 10 (2020): 2384–2402.

17. A. S. Baras, C. Drake, J. J. Liu, et al., “The Ratio of CD8 to Treg Tumor-Infiltrating Lymphocytes Is Associated With Response to Cisplatin-Based Neoadjuvant Chemotherapy in Patients With Muscle Invasive Urothelial Carcinoma of the Bladder,” *Oncoimmunology* 5, no. 5 (2016): e1134412.

18. S. D. Jayasingam, M. Citartan, T. H. Thang, A. A. Mat Zin, K. C. Ang, and E. S. Ch'ng, “Evaluating the Polarization of Tumor-Associated Macrophages Into M1 and M2 Phenotypes in Human Cancer Tissue: Technicalities and Challenges in Routine Clinical Practice,” *Frontiers in Oncology* 9 (2019): 1512.

19. F. Pantano, P. Berti, F. M. Guida, et al., “The Role of Macrophages Polarization in Predicting Prognosis of Radically Resected Gastric Cancer Patients,” *Journal of Cellular and Molecular Medicine* 17, no. 11 (2013): 1415–1421.

20. R. Pampena, G. Parisi, M. Benati, et al., “Clinical and Dermoscopic Factors for the Identification of Aggressive Histologic Subtypes of Basal Cell Carcinoma,” *Frontiers in Oncology* 10 (2020): 630458.

21. J. W. Tjiu, J. S. Chen, C. T. Shun, et al., “Tumor-Associated Macrophage-Induced Invasion and Angiogenesis of Human Basal Cell Carcinoma Cells by Cyclooxygenase-2 Induction,” *Journal of Investigative Dermatology* 129, no. 4 (2009): 1016–1025.

22. I. Elamin, R. D. Zecevic, D. Vojvodic, L. Medenica, and M. D. Pavlovic, “Cytokine Concentrations in Basal Cell Carcinomas of Different Histological Types and Localization,” *Acta Dermatovenerologica Alpina, Pannonica et Adriatica* 17, no. 2 (2008): 55–59.

23. S. H. Bongers, N. Chen, E. van Grinsven, et al., “Kinetics of Neutrophil Subsets in Acute, Subacute, and Chronic Inflammation,” *Frontiers in Immunology* 12 (2021): 674079.

24. N. J. Collier and L. E. Rhodes, “Photodynamic Therapy for Basal Cell Carcinoma: The Clinical Context for Future Research Priorities,” *Molecules* 25, no. 22 (2020): 5398.

25. D. D. Demirseren, C. Ceran, B. Aksam, M. E. Demirseren, and A. Metin, “Basal Cell Carcinoma of the Head and Neck Region: A Retrospective Analysis of Completely Excised 331 Cases,” *Journal of Skin Cancer* 2014 (2014): 858636.

26. J. H. Pyne, E. Myint, E. M. Barr, S. P. Clark, and R. Hou, “Basal Cell Carcinoma: Variation in Invasion Depth by Subtype, Sex, and Anatomic Site in 4,565 Cases,” *Dermatology Practical & Conceptual* 8, no. 4 (2018): 314–319.

Supporting Information

Additional supporting information can be found online in the Supporting Information section. **Figure S1:** Cell classification scheme used with the T-cell multiplex IF panel. **Figure S2:** Cell classification scheme used with the myeloid multiplex IF panel. **Figure S3:** Immunosuppressive ratios (CD8/T-regs and M1/M2 macrophages) at different body sites (head/neck vs. trunk or extremities). **Table S1:** Antigens and fluorophores utilized in the T-cell and myeloid cell multiplex immunofluorescence panels to identify various immune cells. **Table S2:** Overall BCC cohort characteristics, including body site location and histologic subtype.